The Influence of Processing Parameters on the Al-Mn Enriched Nano-Precipitates Formation in a Novel Al-Mn-Cr-Zr Alloy Tailored for Power Bed Fusion-Laser Beam Process

Original
The Influence of Processing Parameters on the Al-Mn Enriched Nano-Precipitates Formation in a Novel Al-Mn-Cr-Zr Alloy Tailored for Power Bed Fusion-Laser Beam Process / Martucci, A., Mehta, B., Lombardi, M., Nyborg, L.. - In: METALS. - ISSN 2075-4701. - ELETTRONICO. - 12:8(2022), p. 1387. [10.3390/met12081387]

Publisher:
MDPI

Published
DOI:10.3390/met12081387

metals
MDPI

Article

The Influence of Processing Parameters on the Al-Mn Enriched Nano-Precipitates Formation in a Novel Al-Mn-Cr-Zr Alloy Tailored for Power Bed Fusion-Laser Beam Process

Alessandra Martucci [1],*, Bharat Mehta [2], Mariangela Lombardi [1] and Lars Nyborg [2]

[1] Department of Applied Science and Technology, Politecnico di Torino, 10129 Turin, Italy
[2] Department of Industrial and Materials Science, Chalmers University of Technology, 412 96 Gothenburg, Sweden
* Correspondence: alessandra.martucci@polito.it

Abstract: Among the recently developed compositions tailored for the power bed fusion-laser beam process (PBF-LB), the novel Al-Mn-Cr-Zr alloy stands out. This composition exploits high solid solution strengthening, achieving a high hardness value in the as-built condition. The produced samples are inherently crack-free and have a good level of densification (~99.5%). The goal of this study is to investigate how this quaternary system is affected by the laser power while retaining a similar volumetric energy density. A comparison between the microstructural features and the mechanical performance was performed on a set of samples processed with power values ranging from 100 to 170 W. Microstructural features were investigated through optical microscopy, Electron Back Scattered Diffraction (EBSD) investigation and feature analysis using advanced microscopy to examine the amount, distribution, and shape of precipitates in the different process conditions. Although the quantitative feature analysis permitted analysis of more than 60 k precipitates for each power condition, all samples demonstrated a low level of precipitation (below 0.3%) with nanometric size (around 75 nm). The mechanical performances of this quaternary system as a function of the laser power value were evaluated with a microhardness test, recording very similar values for the different process conditions with a mean value of approximately 104 HV. The results suggested a very stable system over the tested range of process parameters. In addition, considering the low level of precipitation of nanometric phases enriched in Al-Mn, a supersaturated state could be established in each process condition.

Keywords: PBF-LB; Al-Mn-Cr-Zr; Al-based alloys; feature analysis; Al-Mn precipitates

check for updates

Citation: Martucci, A.; Mehta, B.; Lombardi, M.; Nyborg, L. The Influence of Processing Parameters on the Al-Mn Enriched Nano-Precipitates Formation in a Novel Al-Mn-Cr-Zr Alloy Tailored for Power Bed Fusion-Laser Beam Process. *Metals* **2022**, *12*, 1387. https://doi.org/10.3390/met12081387

Academic Editors: Praveen Sathiyamoorthi and Manogna Karthik Gangaraju

Received: 4 August 2022
Accepted: 16 August 2022
Published: 20 August 2022

1. Introduction

Additive Manufacturing (AM) of metallic materials has attracted a growing and widespread interest in many industrial sectors, thanks to the progress in mechanical control systems and the evolution of advanced energy sources [1]. Among the many AM technologies, the powder bed fusion-laser beam (PBF-LB) process stands out for the possibility to produce complex-shaped functional parts [2]. In this process, the powder bed is melted by a focused laser beam in a layer-wise fashion with extremely high cooling rates (up to 105 K/s) [3]. The increasing interest of industry in high-strength and light-weight materials justifies the boom in demand for Al-based alloys [4]. Although the Al-based alloys are attractive for an excellent strength-to-weight ratio, their PBF-LB processing is often proven to be critical for both printability and strength [5]. The high reflectivity of the Al powder and the high thermal conductivity of the solidified material results in increased power demand [6]. A further significant problem in Al-based alloys processing is the susceptibility to solidification cracking, causing limited fatigue life and mechanical properties in general [7]. In order to improve the Al-based alloys processability, there is a growing body of literature that studies modifications of conventional compositions to make them suitable for PBF-LB production or develops novel compositions tailored to the PBF-LB process [8,9].

Despite pure aluminium being characterized by low yield strength (15 MPa), this can be brought up to 500–600 MPa by alloying [10]. For this reason, it is crucial to think of improved processability while developing novel compositions. The alloying of aluminium is traditionally aimed at exploiting solid solution strengthening, precipitation strengthening and the Hall-Patch effect with grain refinement. The new frontier in the development of tailored Al-based alloys for PBF-LB is the achievement of high supersaturation to exploit the solid solution strengthening in the as-built state and obtain fine and controlled precipitation after heat treatments. Identifying transition elements with a low diffusivity plays a crucial role in slowing down the nucleation and growth kinetics of secondary precipitates formed during PBF-LB remelting [11]. Du et al. studied the bulk diffusivities of different elements in Al at high temperatures (500–700 K) demonstrating that the diffusion coefficients of Fe, Mn, Cr and V are markedly lower than the common elements of Al alloys (Mg, Cu, Si) [12].

The addition of Mn in aluminium alloys was widely discussed due to its excellent workability, weldability, and corrosion resistance [13–18]. The presence of Mn in solid solution proved to be an excellent example for strengthening Al alloys [14]. In addition, the rapid solidification achieved during the PBF-LB process results in an extended Mn solubility [15]. As observed by Jia et al., the PBF-LB extremely high cooling rate can in fact retain up to 4.3 wt% of Mn in supersaturated solid solution, which greatly exceeds its equilibrium solubility (approx. 1.8 wt%) [16]. Along the grain boundaries, Mn-rich particles were found to play a role in delaying grain growth during the process [17]. However, as better explained by Kimura et al., an intensive grain refinement was not detected in the binary Al-3Mn, possibly due to the low solid solubility limits of Mn in aluminium alloys [18]. Nevertheless, Hori et al. demonstrated that grain refinement occurred when a small amount of chromium was added to rapidly solidified aluminium alloys [19]. Increasing attention was also paid to the addition of Zr into Al-based alloys due to its ability to be a good inoculant creating a very fine microstructure. Al_3Zr precipitates are in fact known to be very effective in preventing recrystallization, even at high temperatures and to reduce coarsening kinetics [20].

Among the many tried and tested compositions containing Mn, Cr and Zr, the novel Al-Mn-Cr-Zr alloy designed by Mehta et al. stands out [21]. Combining solid solution and precipitation strengthening, crack-free and high-strength samples were produced. Despite most of the alloying elements being preserved in solid solution, Mn-rich nanometric precipitates were observed along melt pool boundaries and grain boundaries, probably caused by the re-melting phenomenon. However, in order to overcome the problem of high reflectivity in aluminium, only the maximum value of the PBF-LB machine (170 W) was tested in their work and investigations at lower powers to minimise the effect of re-melting were not conducted. In addition, the amount and size distribution of these precipitates were not established in their work.

The aim of the present work was to investigate the effect of the used power value on the Al-Mn-Cr-Zr system. For this purpose, 100, 125, 150 and 170 W were set as power values for the bulk production with the volumetric energy density (VED) fixed around 37 Jmm^{-3}. Moreover, the amount and size distribution of Al-Mn nano-precipitates were investigated in-depth, in order to understand how their formation is affected by varying power and how their presence influences the mechanical properties of the alloy.

2. Materials and Methods

2.1. Material

For this study, gas atomized Al-Mn-Cr-Zr powder provided by Höganäs AB, Höganäs, Sweden was selected. The alloy chemical composition based on ICP-AES values is reported in Table 1.

Table 1. Al-Mn-Cr-Zr chemical composition.

Element (wt%)	Mn	Cr	Zr	Fe	Si	Al
Al-Mn-Cr-Zr	5.0	0.8	0.59	0.16	0.16	Remainder

As it is possible to observe in the Scanning Electron Microscope (SEM) micrograph (Figure 1), the provided powder is characterized by particles with a spherical shape. The particle size distribution parameters, reported in Figure 1, were measured by Malvern, UK, at RISE, Mölndal using a Mastersizer 3000.

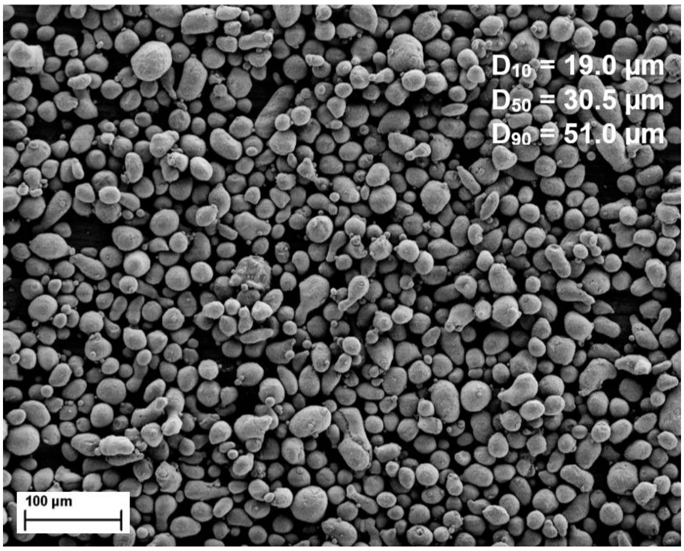

Figure 1. Powder morphology observed with SEM with powder size distribution reported.

2.2. PBF-LB Processing

$10 \times 10 \times 10$ mm^3 cubic samples were built using an EOS M100 machine from EOS GmbH, Krailling, Germany. This is a PBF-LB system with a cylindrical build volume of 100 mm as diameter and 100 mm as height equipped with a Yb-fibre laser with a spot size of 40 µm and a maximum power of 200 W (nominal 170 W). Before proceeding with the PBF-LB production of the samples, the powder was dried at 353 K for 4 h. All samples were produced with a layer thickness of 30 µm and a hatch distance (hd) of 100 µm. 100, 125, 150 and 170 W were selected as power values resulting in a VED fixed at approximately 37 Jmm^{-3}, applying Equation (1).

$$VED = \frac{P}{l \times hd \times v} \tag{1}$$

The parameters used for bulk production are summarised in Table 2.

Table 2. PBF-LB parameters.

Power (W)	Hatch Distance (mm)	Layer Thickness (µm)	Scan Speed (mm/s)	VED (Jmm^{-3})
100	0.1	30	875	37
125	0.1	30	1125	
150	0.1	30	1375	
170	0.1	30	1500	

2.3. Characterization

The as-built samples were cut from the build platform using a cold saw along the planes indicated in Figure 2.

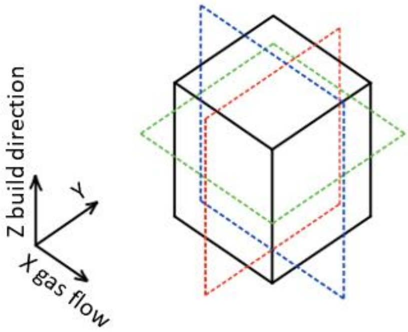

Figure 2. Cutting planes used for samples preparation.

After cutting, all the samples were mounted on a conductive resin called Polyfast (from Struers, Copenaghen, Denmark). Then all the cut samples were polished using Struers' standard metallographic procedure for Al-Si cast alloys [22]. The relative density was determined using a ZEISS Axioscope 7 (Zeiss, Wetzlar, Germany) optical microscope (OM) by image analysis. With this instrument, it was possible to create a stitched version of images taken of the entire samples with an optical zoom of 10×. After obtaining stitched images for XZ, YZ and XY planes of each process condition, these were processed using ImageJ (1.52t version, developed by National Institutes of Health, Bethesda, Rockville, MD, USA) in order to obtain the percentage of pores area and thus the relative density value of each sample. To make the melt pools visible to the OM, the samples were etched for 8–10 s with Keller's reagent (90 mL water, 2.5 mL HNO_3, 1.5 mL HCl and 1 mL HF) following the standard procedure for Al-based alloys. Since the power affects the shape and depth of the melt pool, a morphological investigation was carried out by means of an OM analysis on etched samples. Ten measures for each process condition were performed. The measurements were all taken on the last printed layer as it had not been affected by re-melting. A Zeiss Gemini 450 SEM (Zeiss, Wetzlar, Germany) with back scattered electron (BSE) detector was used in combination with AZtec v5.0 software by Oxford Instruments, Abingdon-on-Thames, UK for the analysis of precipitates. This software performs the feature analysis, identifying precipitates as grey contrast. To perform the feature analysis, the SEM was set at 5 kV with 2 nA as probe current, and the imaging was done at 1024 resolution. The area selected for each process condition was 0.3×0.3 mm^2 and 10k was set as magnification which permitted detection of a 30 nm feature as a minimum feature. The X-Ray Diffraction (XRD) analyses were conducted at Höganäs AB, Höganäs, Sweden at 45 kV and 40 mA in a Bragg Brentano configuration, with a Cu source ($K\alpha$ = 1.5406 Å). A step size of 0.007°, a time step of 1 s and a 2θ range between 20° and 100° were considered for the full pattern. After that, a detailed analysis was conducted in a limited area of the pattern using 2θ = 37.5–45.6°, step size = 0.003° and time per step = 1 s. The Zeiss Gemini 450 SEM was equipped with a symmetry EBSD detector (Oxford Instruments, Abingdon-on-Thames, UK) and analysed using the Aztec software. EBSD orientation maps were recorded at 250× magnification and a step size of 1 µm. The SEM was operating at 10 kV and 5 nA and the samples were used in a pre-tilted sample holder at 70° tilt. The working distance for EBSD was kept around 15 mm. Hardness tests were carried out in order to investigate the mechanical behaviour for each process condition. The microhardness tests were performed as per ASTM standards E92, E384 on all the samples using a DuraScan system (from Struers, Copenaghen, Denmark). The microhardness analysis was carried out keeping sixteen measurements for each XZ and XY plane and setting a load of 0.3 kg with a hold time of 10 s.

3. Results

3.1. Relative Density at Different Processing Parameters

The relative density of each sample built was firstly examined as a power function and the results are summarized in Figure 3.

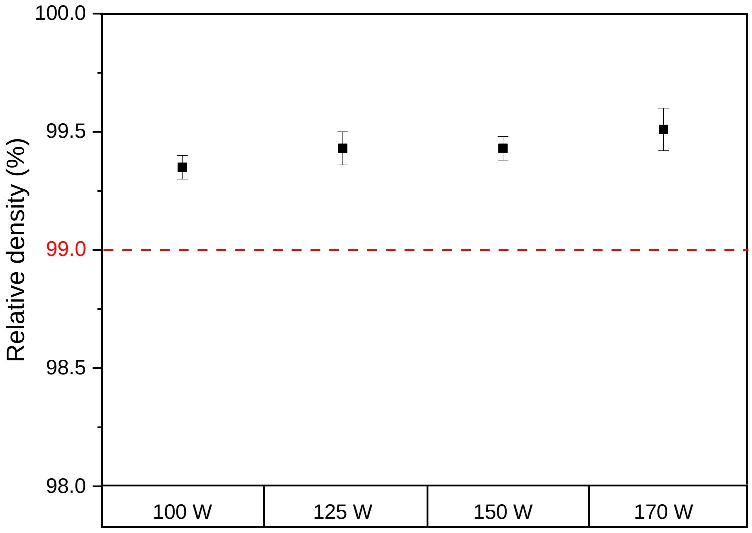

Figure 3. Relative density of the Al-Mn-Cr-Zr samples at various power values.

As inferred from Figure 3, a slightly increasing trend can be noticed as the power increases but a good level of densification (over 99%) was achieved for all processing conditions. In addition, all samples proved to be crack-free.

3.2. Melt Pool Morphology and Depth

Figure 4 shows the metallographic images in the XZ section of etched samples produced with different process conditions.

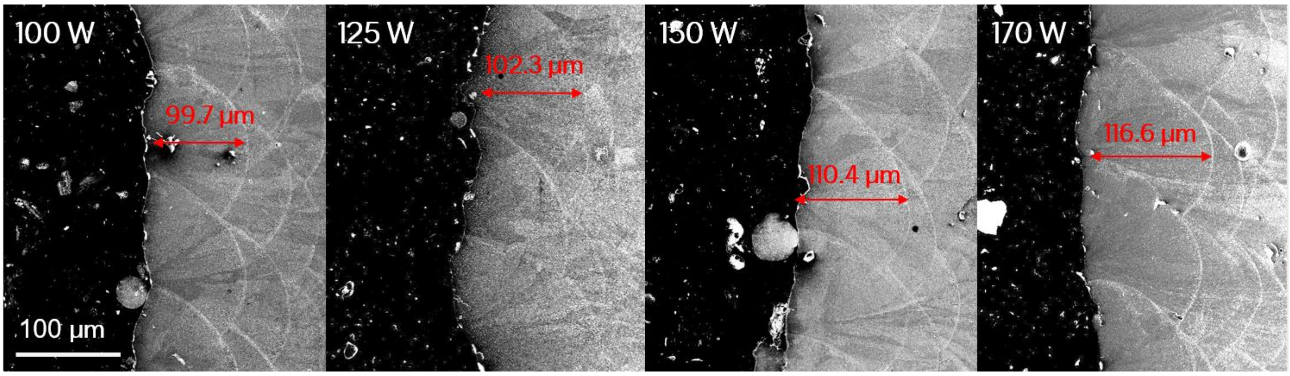

Figure 4. Metallographic images on XZ plane as a function of used power values. The mean melt pool depths are indicated in red.

The shape of the melt pool changes according to the different power values. Notwithstanding the measurements were taken in the last layer to avoid the remelting phenomenon and to clearly see the entire melt pool, the melt pools overlapped across the width due to the hatch distance (hd) set on 100 µm during the PBF-LB sample production. With these considerations, only the depths of the melt pools were measured and reported in Figure 5. In particular, it is possible to note that lower power results in shorter melt pools, while higher power results in longer melt pools.

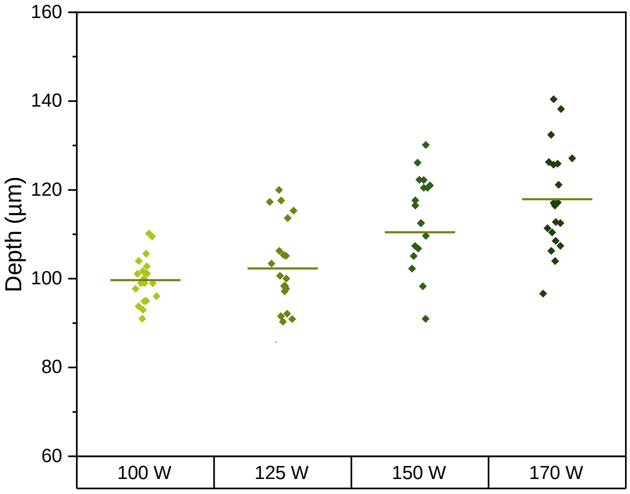

Figure 5. Results of melt pool morphology investigation as a function of laser power value used.

The standard deviations are quite large for each process condition probably due to the irregularity of the last layer and the rotated scanning strategy. The latter results in an analysis plane that is not always perpendicular to the melt pool. However, a rising trend in both mean value and positive standard deviation with the increase in power could be noticed and explained by the remelting phenomenon that occurs at higher laser power.

3.3. Microstructural Investigation

In order to assess any change in grain size or orientation, the EBSD investigations were conducted and the results are reported in Figure 6. The majority of grains extend across several layers and grow along the building direction as demonstrated by the pole figures. A strong [100] orientation was in fact recorded in each sample. As indicated by the black arrows, rare randomly distributed melt pools reveal grain refinement along the grain boundaries in samples produced up to 150 W. In contrast, no evident refinement was noted for the sample produced at the highest power.

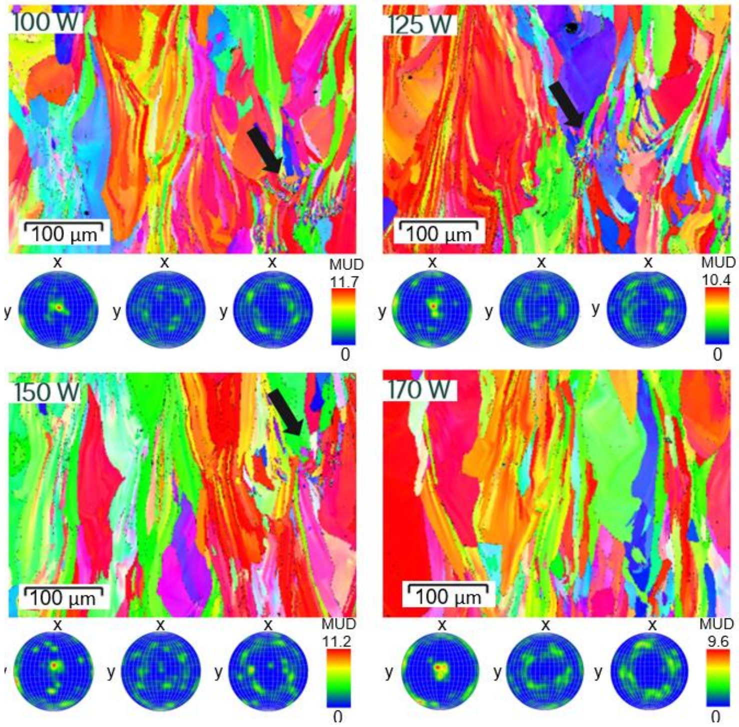

Figure 6. EBSD maps related to all power conditions.

From the EBSD maps, grain sizes were analysed as a function of the equivalent circular diameter (ECD) index. The frequency reported in Figure 7 is a numeric frequency based on counting. As displayed in Figure 7, some differences in terms of grain size distribution can be found for samples processed with the four power values. In particular, with increased power values the contribution of finer grains markedly decreases (as indicated from the arrow in Figure 7). In addition, a peak at ECD of 25 µm appears increasingly marked as the used power increases.

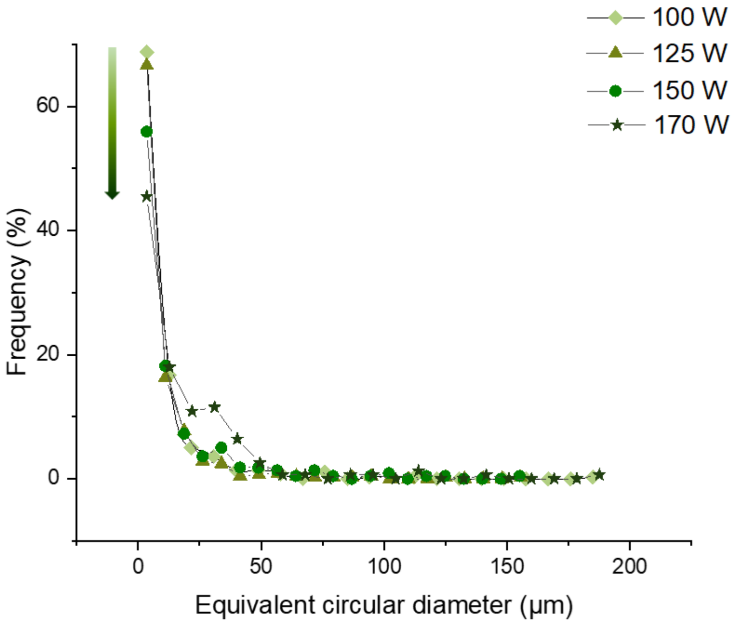

Figure 7. Grain size distribution as a function of power value.

All samples were also characterised with SEM in back scattered mode to recognize the grain contrast and the precipitate contrast as a grey contrast. In Figure 8, by way of example, only the SEM micrograph of a low power specimen was reported since no significant differences were noticed for the other microstructures.

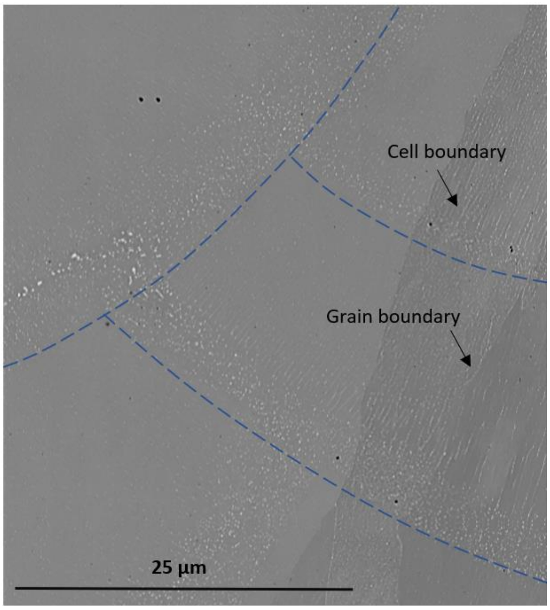

Figure 8. SEM micrographs of as-built PBF-LB processed Al-Mn-Cr-Zr. Melt pool boundaries marked in blue.

The SEM analysis on the XZ plane revealed two categories of precipitates with different morphology and location in the microstructure. In Figure 8, numerous spherical precipitates are observed on the melt pool boundaries (marked in blue). In contrast, fewer precipitates with more oblong shapes seem to form on the grain and cell boundaries (indicated with black arrows). The quantitative and morphological analysis of precipitates was conducted using the Aztec software on 0.3 × 0.3 mm^2 for each XZ sample. In Figure 9 the precipitates aspect ratio (AR) distributions were reported for each power condition. The AR is a function of the largest diameter and the smallest diameter orthogonal to it commonly used as a shape factor in particle analysis. The AR varies from close to one for perfectly spherical precipitate particles to higher values for more elongated ones. The graph displays no variation as the power varies. In particular, three main peaks can be highlighted: the most pronounced at 1.15 revealing nearly spherical particles, a minor peak at 1.7 denoting more elongated precipitates and a less pronounced one at about 2 indicating very elongated particles. The shape of the precipitates correlated to each peak is displayed in Figure 9.

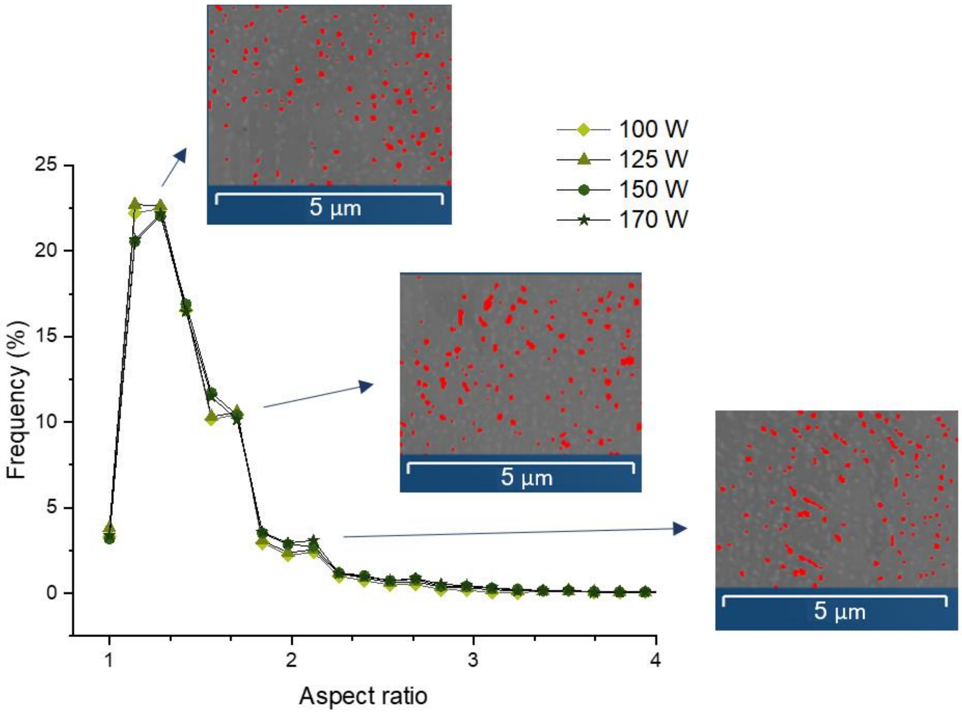

Figure 9. Precipitates aspect ratio distribution and Aztec images for each power condition.

Considering the pronounced peak close to unity and with the aim to simplify the data interpretation, the precipitates were evaluated as spherical particles. Therefore, the precipitates size distributions were reported as ECD function in Figure 10.

Observing Figure 10, the ECD are mainly in a range of 0.03–0.5 µm for each power condition. The main peak is centred around 0.075 µm of ECD for each process condition. Although samples built with 125 and 150 W exhibit an identical trend, the specimens with the lowest and highest power show slightly different trends. In particular, the sample produced with 100 W shows a global increase in the number of precipitates and a very pronounced peak for small precipitates. Moreover, the sample produced with the highest power (170 W) has a further small peak around 0.2 µm. In order to quantify the precipitation contribution for all different process conditions, the portion of the area covered by precipitates in relation to the total analysed area (0.3 × 0.3 mm^2) was assessed and reported in Figure 11.

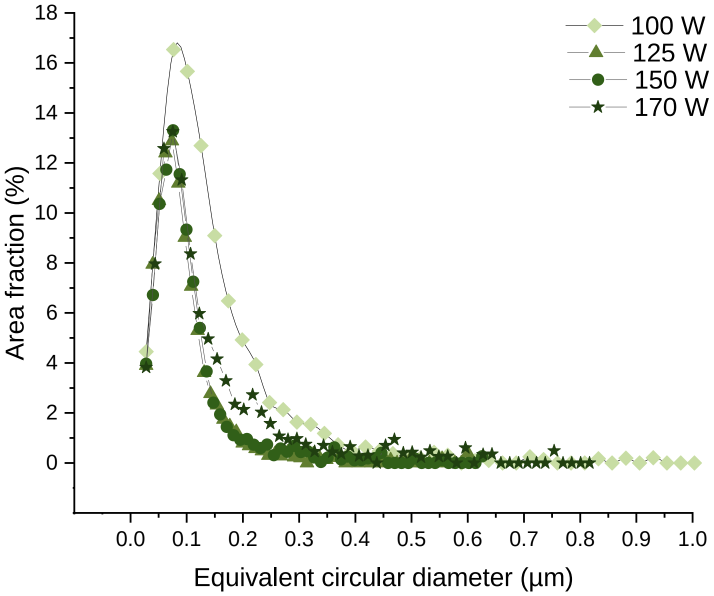

Figure 10. Power-dependent size distribution of spherical precipitates.

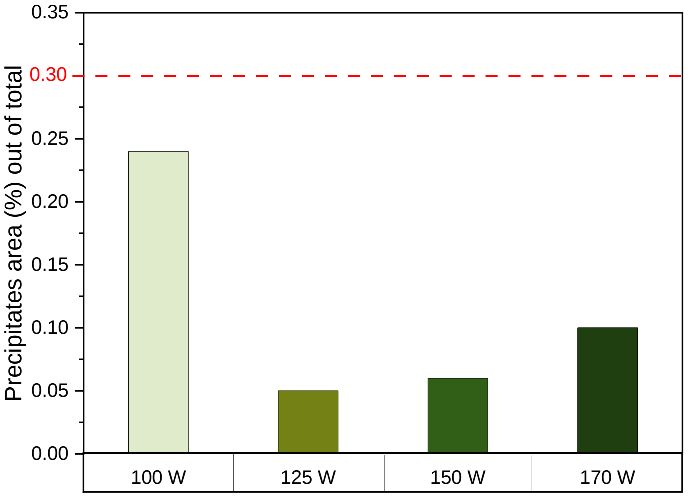

Figure 11. Percentage of the analysed area covered by precipitates.

Higher precipitation in the sample produced at 100 W is evident from the graph in Figure 11. A growing trend is then visible between 125 and 170 W. It is important to note that for all conditions the precipitation is below 0.3% and thus extremely low.

3.4. Phase Identification

A preliminary XRD investigation was carried out on all samples processed with four power conditions. According to Figure 12a, in this generic analysis no considerable differences in the patterns can be noticed. In order to make the smallest peaks more visible and to easily understand if phase differences can be found varying process parameters, a more accurate and focused scan was carried out (Figure 12b).

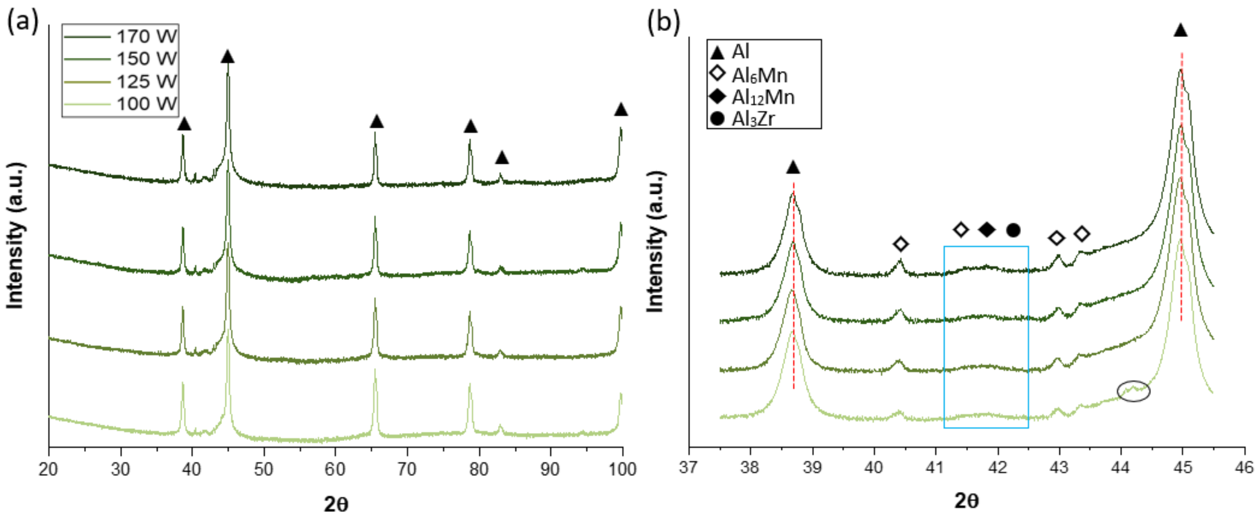

Figure 12. The complete XRD patterns for each power condition (**a**) and the detailed analysis in a 2ϑ range of 37.5–45.5° (**b**).

The two main peaks shown in Figure 12b are centred at 38.6° and 45.2° respectively and for them no marked shift can be observed when the used powder value is changed. However, a slightly pronounced hump (probably a combination of peaks) can be detected around 41.7° and its intensity rises with increasing power (blue rectangle in Figure 12b). Furthermore, as highlighted by the black circle in Figure 12b, an additional peak at around 44.2° is found in the 100 W pattern. An accurate analysis using HighScore software (v4.0, Malvern Panalytical, Malvern, UK) revealed that these peaks are attributable to Al-Mn phases with various stoichiometric coefficients (Al_6Mn and $Al_{12}Mn$) and Al_3Zr phase.

3.5. Microhardness Testing

The mechanical properties were investigated by performing Vickers microhardness tests on XZ and XY planes for each sample. As no difference was highlighted between the two planes of all samples, the average results with their standard deviations were reported in Figure 13. A mean microhardness value of about 104.5 HV was recorded on all samples. The slight variations that can be noticed in varying power values become insignificant when the standard deviations and the intrinsic measurement errors are considered.

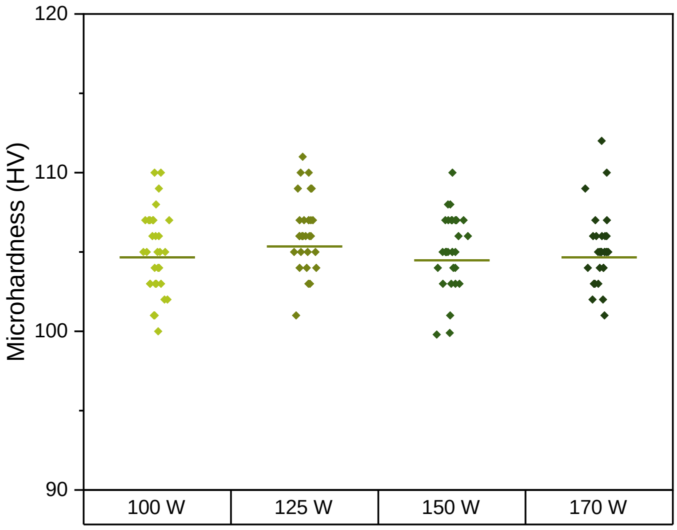

Figure 13. Results of Vickers microhardness tests for each power condition.

4. Discussion

As it is widely known for Al-Mn or Al-Cr based systems, solid solutions containing much more than the equilibrium limit of manganese or chromium in aluminium can be obtained by rapid solidification [15]. Considering the low bulk diffusivity of Mn and Cr, the rapid solidification process can produce highly concentrated Al-Mn or Al-Cr based alloys restricting precipitation [12,18]. By exploiting the high cooling rates of the PBF-LB process, a supersaturated state can be in fact induced in the as-built state. Additionally, Mn and Cr have high lattice misfits, thus providing a strong solid solution effect. This condition, after heat treatment, leads to the controlled formation of finely dispersed precipitates [23]. On the basis of these potentialities, several Al-Mn systems have been studied and, among the many, the Al-Mn-Cr-Zr developed by Mehta et al. stands out [21]. In the work of Mehta et al. the nominal power of their PBF-LB machine (170 W) was set to deal with the high reflectivity of aluminium, but Mn-rich particles precipitated to a certain finite extent during the AM process [21]. The purpose of the present study was to understand if there is a difference in microstructure in terms of amount of precipitation, supersaturation in the matrix, and texture generated at different power regimes. For this purpose, 100, 125, 150 and 170 W were set as power values for the sample production with the VED fixed at 37 $\mathrm{Jmm^{-3}}$. Samples processed with all power conditions demonstrated a very good level of densification (around 99.5%).

As extensively discussed in literature, the process parameters significantly influence the scanning depth and thus the morphology of the melt pool [24–26]. In order to investigate this phenomenon, a study of the melt pool morphology was carried out through an optical microscope analysis on etched samples. Considering evidence from the literature, power impacts melt pool morphology considerably more than scan speed [24,26]. For this reason, the study of the melt pool morphology was performed only considering the powder values used. According to Figures 4 and 5, the depth measurements in the last layer revealed an increase in depth when the power used increased. This perfectly aligns with the PBF-LB scan theory of deeper melt pools for higher power and shallower melt pools for lower power [26]. However, the differences in melt pool depths were not extremely pronounced, which can be justified since the VED was kept constant. Moreover, the standard deviations reported in Figure 5 increased with the power used and this is due to the increasing uneven layer production probably caused by the remelting phenomenon of the previous layers.

The remelting phenomenon noticed through melt pools investigations in the sample built with 170 W was confirmed with the EBSD analysis. In fact, if some grain refinement phenomena at the melt pools boundaries were detected in EBSD maps at lower powers (Figure 6), these were not observed in the sample produced at 170 W, supporting the remelting thesis. However, in the lower power samples, the refinement was only noted in a few random melt pools in contrast to what was expected due to the alloyed Zr. An important body of literature studied as the presence of Zr in Al base alloys results in the formation of the inoculant phase Al_3Zr [27–29]. However, the percentage of Zr is a crucial factor to consider because by increasing the percentage of Zr above 0.77 wt% grain refinement was noted [30]. The analysed composition has a Zr content of 0.59 wt% because grain refinement was not strictly desired when this alloy variant was developed. Nevertheless, as proved in other published papers, another important condition for enhancing the effect of Al_3Zr as inoculant phase, is the presence of alloyed Mg, which is not present in the composition studied in the present work [16,31]. Future investigations to attribute the real causes of the random grain refinement need to be conducted. Displaying the grain sizes as a function of the ECD, no significant difference was found for the two lower power values. Nevertheless, when the power increases, the number of more refined grains markedly decreases and the contribution of grains with ECD between 25 and 40 µm increases (Figure 7). These considerations could support the assumption of the remelting phenomenon occurring at high powers.

The microstructural evaluation continued with a feature analysis of Mn-rich precipitates for each explored power condition. In line with what was observed by Mehta et al., numerous spherical precipitates were observed on the melt pool boundaries and a lower number of precipitates with an elongated shape were identified along the grain and cell boundaries (as indicated in Figure 8) [21]. The conducted quantitative feature analysis permitted analysis of more than 60 k precipitates for each power condition. When the precipitate's aspect ratio distributions were displayed as a function of power value, no variation can be observed changing the process conditions. The trends revealed three main peaks: the most pronounced at 1.15 AR correlating with nearly spherical particles, a minor peak at 1.7 AR denoting more elongated precipitates and a less pronounced peak at about 2 AR indicating very elongated particles (Figure 9). The results corroborate the optical analysis and align with the observations of Mehta et al. [21]. The precipitates size distribution, reported in Figure 10, showed similar trends for the 125 and 150 W processed samples, but separate considerations are needed for the lowest and highest power samples. Looking closer, an overall increase in the number of precipitates and a very pronounced peak for small precipitates were found in the sample made at 100 W. This can be correlated to the additional peak around 44.2° found in the XRD pattern of Figure 12 which is not visible in higher power samples. Moreover, a small additional peak around 0.2 µm was visible for the sample built at the highest power (170 W). This could be caused by the increased precipitation of a new class of Mn-rich precipitates formed as a result of the remelting phenomenon occurring with higher powers. This is in line with what was observed during the XRD analysis where a small hump (or set of peaks) around 41.7° became more evident by raising the power (Figure 12). However, it is important to point out that the trend resulting from the quantity analysis showed a level of precipitation significantly below 0.3% for every condition, as highlighted in Figure 11.

Considering the low level of precipitation, the differences observed during the feature analysis in the precipitation reactions are not reflected in the recorded mechanical performance. In fact, the hardness response, reported in Figure 13, was revealed to not be power sensitive. The recorded hardness mean values appear considerably high (104.5 HV) and in line with that reported by Mehta et al. [21].

All these considerations indicate that, with the fixed VED value (37 Jmm^{-3}), a supersaturation condition can be reached regardless of the power values used during the PBF-LB process. In fact, the system proved to be non-power sensitive, achieving densification, microstructural and mechanical properties that are well suited to future heat treatment developments. Achieving a predominantly supersaturated condition in the as-built state with extremely limited nanoscale precipitation is an optimal condition for the development of fast and effective heat treatments. Under these assumptions, a time-consuming and energy-intensive treatment such as solubilisation is not considered necessary and faster heat treatments such as direct aging can be attempted in future studies.

5. Conclusions

A growing body of literature recognises the importance of solid solution strengthening for the Al-based system. The aim of most research is to find new compositions by adding solutes with low diffusion coefficients in order to obtain an as-built supersaturated composition without precipitation. Among many, the high-performance Al-Mn-Cr-Zr alloy stood out. The main goal of the current study was to determine if there is a correlation between the power used and the microstructural and mechanical features of the alloy. For this purpose, the starting point for the present study was the power used in the work of Mehta et al. (170 W) and three additional powers were investigated: 100, 125 and 150 W.

After extensive microstructural investigations and Vickers tests, the following conclusions can be drawn:

- All the examined process parameters resulted to be optimal for the achievement of a high level of densification (around 99.5%);
- Melt pool analysis on etched samples revealed the presence of narrower and deeper melt pools for high power samples and wider and shallower ones for low power samples;
- EBSD analysis revealed longitudinal grain growth on multiple layers along the build direction for each condition. Some randomly diffused grain refinement zones were observed in lower power conditions;
- During the SEM feature analysis, a certain number of precipitates were observed and analysed in terms of amount, shape and distribution. Through the aspect ratio examination, the Al-Mn enriched precipitates can be divided into two categories: the spherical ones plentiful on the melt pool boundaries and the oblong ones observed along the grain and cell boundaries. Quantitative analysis revealed an overall higher number of fine precipitates for the lower power sample in line with the XRD observations. The presence of an additional peak of around 0.2 µm as ECD in the sample produced at 170 W denotes a slightly different precipitation behaviour also confirmed by XRD analysis;
- The slight differences noted in grain distribution and in precipitation behaviour do not affect the hardness properties of the alloy. A constant mean value of 104.5 HV was recorded for all conditions.

Although more than 60 k precipitates were detected and studied for each power condition, the area covered by precipitates out of the total analysed area was always considerably less than 0.3%. So, it is possible to deduce that supersaturation was reached for all samples. The nearly complete supersaturation condition with minimal precipitation of extremely fine and well-dispersed precipitates represents an optimal starting point for future heat treatment developments. Rapid heat treatments such as direct aging are particularly suitable with this as-built microstructural condition and time-consuming and energy-intensive heat treatments such as solubilisation can be skipped. Furthermore, since the microstructural and mechanical results have not shown substantial differences, it is possible to conclude that the alloy is very stable for the set VED. Therefore, selecting the highest power condition is a time-saving choice because it would lead to a higher build rate from the printing process.

Author Contributions: Conceptualization, M.L. and L.N.; methodology, A.M. and B.M.; validation, A.M. and B.M.; investigation, A.M.; resources, L.N.; writing—original draft preparation, A.M.; writing—review and editing, A.M., B.M., M.L. and L.N.; supervision, M.L. and L.N.; project administration, L.N. All authors have read and agreed to the published version of the manuscript.

Funding: This work was funded by European Union's Horizon 2020 research and innovation programme, grant number 820774 within project MANUELA—Additive Manufacturing using Metal Pilot Line. This work was also funded by the Centre for Additive Manufacturing—Metal (CAM2), supported by the Swedish Governmental Agency of Innovation Systems (Vinnova) under grant number 2016-05175.

Institutional Review Board Statement: Not applicable.

Informed Consent Statement: Not applicable.

Data Availability Statement: Not applicable.

Acknowledgments: The authors would like to acknowledge Production Area of Advance at Chalmers University of Technology and LIGHTer academy. Sven Bengtsson at Höganäs AB is acknowledged for help procuring the powder. Björn Skårman at Höganäs AB is acknowledged for conducting X-ray diffraction experiments and their interpretations.

Conflicts of Interest: The authors declare no conflict of interest.

References

1. Herzog, D.; Seyda, V.; Wycisk, E.; Emmelmann, C. Additive manufacturing of metals. *Acta Mater.* **2016**, *117*, 371–392. [CrossRef]
2. Yao, J.; Ding, R.; Li, K.; Du, B.; Zhao, L.; Yuan, Y. Study on the impact behavior of arch micro-strut (ARCH) lattice structure by selective laser melting (SLM). *Rapid Prototyp. J.* **2022**, *28*, 1541–1557. [CrossRef]
3. Rometsch, P.; Jia, Q.; Yang, K.V.; Wu, X. Aluminum alloys for selective laser melting–towards improved performance. In *Additive Manufacturing for the Aerospace Industry*; Elsevier: Amsterdam, The Netherlands, 2019; pp. 301–325. [CrossRef]
4. Xiao, H.; Zhang, C.; Zhu, H. Effect of direct aging and annealing on the microstructure and mechanical properties of AlSi10Mg fabricated by selective laser melting. *Rapid Prototyp. J.* **2022**. ahead of print. [CrossRef]
5. Aversa, A.; Marchese, G.; Saboori, A.; Bassini, E.; Manfredi, D.; Biamino, S.; Lombardi, M. New aluminum alloys specifically designed for laser powder bed fusion: A review. *Materials* **2019**, *12*, 1007. [CrossRef] [PubMed]
6. Patel, S.; Chen, H.; Vlasea, M.; Zou, Y. The influence of divergent laser beams on the laser powder bed fusion of a high reflectivity aluminium alloy. *arXiv* **2021**. [CrossRef]
7. Stopyra, W.; Gruber, K.; Smolina, I.; Kurzynowski, T.; Kuźnicka, B. Laser powder bed fusion of AA7075 alloy: Influence of process parameters on porosity and hot cracking. *Addit. Manuf.* **2020**, *35*, 101270. [CrossRef]
8. Montero-Sistiaga, M.L.; Mertens, R.; Vrancken, B.; Wang, X.; van Hooreweder, B.; Kruth, J.P.; van Humbeeck, J. Changing the alloy composition of Al7075 for better processability by selective laser melting. *J. Mater. Process. Technol.* **2016**, *238*, 437–445. [CrossRef]
9. Zhang, H.; Zhu, H.; Nie, X.; Yin, J.; Hu, Z.; Zeng, X. Effect of Zirconium addition on crack, microstructure and mechanical behavior of selective laser melted Al-Cu-Mg alloy. *Scr. Mater.* **2017**, *134*, 6–10. [CrossRef]
10. Mertens, R.; Baert, L.; Vanmeensel, K.; van Hooreweder, B. Laser powder bed fusion of high strength aluminum. *Mater. Des. Process. Commun.* **2021**, *3*, e161. [CrossRef]
11. Furrer, P.; Warlimont, H. Microstructure and properties of aluminum alloys after rapid solidification. Li. Extension of solid solubility, influence of thermal treatments, mechanical properties. *Z. Met.* **1971**, 100–112.
12. Du, Y.; Chang, Y.A.; Huang, B.; Gong, W.; Jin, Z.; Xu, H.; Yuan, Z.; Liu, Y.; He, Y.; Xie, F.Y. Diffusion coefficients of some solutes in fcc and liquid Al: Critical evaluation and correlation. *Mater. Sci. Eng. A* **2003**, *363*, 140–151. [CrossRef]
13. Polmear, I.; StJohn, D.; Nie, J.F.; Qian, M. *Light Alloys: Metallurgy of the Light Metals*; Butterworth-Heinemann: Oxford, UK, 2017.
14. Rometsch, P.A.; Zhu, Y.; Wu, X.; Huang, A. Review of High-Strength Aluminium Alloys for Additive Manufacturing by Laser Powder Bed Fusion. *Mater. Des.* **2022**, *219*, 110779. [CrossRef]
15. Shechtman, D.; Schaefer, R.J.; Biancaniello, F.S. Precipitation in rapidly solidified Al-Mn alloys. *Metall. Trans. A* **1984**, *15*, 1987–1997. [CrossRef]
16. Jia, Q.; Rometsch, P.; Kürnsteiner, P.; Chao, Q.; Huang, A.; Weyland, M.; Bourgeois, L.; Wu, X. Selective laser melting of a high strength AlMnSc alloy: Alloy design and strengthening mechanisms. *Acta Mater.* **2019**, *171*, 108–118. [CrossRef]
17. Bayoumy, D.; Schliephake, D.; Dietrich, S.; Wu, X.H.; Zhu, Y.M.; Huang, A.J. Intensive processing optimization for achieving strong and ductile Al-Mn-Mg-Sc-Zr alloy produced by selective laser melting. *Mater. Des.* **2021**, *198*, 109317. [CrossRef]
18. Kimura, T.; Nakamoto, T.; Ozaki, T.; Miki, T. Microstructures and mechanical properties of aluminum-transition metal binary alloys (Al-Fe, Al-Mn, and Al-Cr) processed by laser powder bed fusion. *J. Alloys Compd.* **2021**, *872*, 159680. [CrossRef]
19. Hori, S.; Matsumoto, E.; Tai, H.; Furushiro, N.; Sasaki, A. Precipitation Behavior Aging of Rapidly Solidified Al–Cr Alloys. *J. Jpn. Inst. Light Met.* **1988**, *38*, 147–152. [CrossRef]
20. Spierings, A.B.; Dawson, K.; Voegtlin, M.; Palm, F.; Uggowitzer, P.J. Microstructure and mechanical properties of as-processed scandium-modified aluminium using selective laser melting. *CIRP Ann.* **2016**, *65*, 213–216. [CrossRef]
21. Mehta, B.; Nyborg, L.; Frisk, K.; Hryha, E. Al–Mn–Cr–Zr-based alloys tailored for powder bed fusion-laser beam process: Alloy design, printability, resulting microstructure and alloy properties. *J. Mater. Res.* **2022**, *37*, 1256–1268. [CrossRef]
22. Streurs. Metallographic Preparation of Aluminum and Aluminum Alloys. Available online: https://www.struers.com/en/Knowledge/Materials/Aluminum#preparationmethod (accessed on 29 September 2021).
23. Fiocchi, J.; Tuissi, A.; Biffi, C.A. Heat treatment of aluminium alloys produced by laser powder bed fusion: A review. *Mater. Des.* **2021**, *204*, 109651. [CrossRef]
24. Cheng, B.; Lydon, J.; Cooper, K.; Cole, V.; Northrop, P.; Chou, K. Melt pool sensing and size analysis in laser powder-bed metal additive manufacturing. *J. Manuf. Process.* **2018**, *32*, 744–753. [CrossRef]
25. Khorasani, M.; Ghasemi, A.; Leary, M.; Sharabian, E.; Cordova, L.; Gibson, I.; Downing, D.; Bateman, S.; Brandt, M.; Rolfe, B. The effect of absorption ratio on meltpool features in laser-based powder bed fusion of IN718. *Opt. Laser Technol.* **2022**, *153*, 108263. [CrossRef]
26. Lane, B.; Zhirnov, I.; Mekhontsev, S.; Grantham, S.; Ricker, R.; Rauniyar, S.; Chou, K. Transient laser energy absorption, co-axial melt pool monitoring, and relationship to melt pool morphology. *Addit. Manuf.* **2020**, *36*, 101504. [CrossRef] [PubMed]
27. Fuller, C.B.; Seidman, D.N.; Dunand, D.C. Mechanical properties of Al (Sc, Zr) alloys at ambient and elevated temperatures. *Acta Mater.* **2003**, *51*, 4803–4814. [CrossRef]
28. Spierings, A.B.; Dawson, K.; Uggowitzer, P.J.; Wegener, K. Influence of SLM scan-speed on microstructure, precipitation of Al3Sc particles and mechanical properties in Sc-and Zr-modified Al-Mg alloys. *Mater. Des.* **2018**, *140*, 134–143. [CrossRef]
29. Martucci, A.; Aversa, A.; Manfredi, D.; Bondioli, F.; Biamino, S.; Ugues, D.; Lombardi, M.; Fino, P. Low-Power Laser Powder Bed Fusion Processing of Scalmalloy®. *Materials* **2022**, *15*, 3123. [CrossRef]

30. Griffiths, S.; Rossell, M.D.; Croteau, J.; Vo, N.Q.; Dunand, D.C.; Leinenbach, C. Effect of laser rescanning on the grain microstructure of a selective laser melted Al-Mg-Zr alloy. *Mater. Charact.* **2018**, *143*, 34–42. [CrossRef]
31. Croteau, J.R.; Griffiths, S.; Rossell, M.D.; Leinenbach, C.; Kenel, C.; Jansen, V.; Seidman, D.N.; Dunand, D.C.; Vo, N.Q. Microstructure and mechanical properties of Al-Mg-Zr alloys processed by selective laser melting. *Acta Mater.* **2018**, *153*, 35–44. [CrossRef]